



## Research Article

## Generation and characterization of an improved carbon fiber model by molecular dynamics



Linyuan Shi , Marina Sessim , Michael R. Tonks , Simon R. Phillpot \*

Department of Materials Science and Engineering, University of Florida, Gainesville, FL, 32611, USA

## ARTICLE INFO

## Article history:

Received 25 August 2020

Received in revised form

2 November 2020

Accepted 3 November 2020

Available online 6 November 2020

## Keywords:

Molecular dynamics  
Carbon fiber  
Characterization

## ABSTRACT

A high-fidelity model is necessary for understanding the properties of carbon fibers (CFs) and developing the next generation of CFs and related composites. Using kinetic Monte Carlo combined with large-scale Molecular Dynamics (kMC-MD), we generate two types of CF models at a wide range of initial densities (from 1.2 g/cm<sup>3</sup> to 2.0 g/cm<sup>3</sup>). These fiber core and thin fiber models represent a small section of interior region of large fiber and a very thin carbon fiber with a well-defined surface, respectively. The microstructures of the fiber core and thin fiber are characterized in terms of their shapes, densities, pore size distribution and hybridization of carbon atoms. We find both the fiber core and thin fiber models have densities and structural characteristics similar to experimental structures. Further, the virtual X-ray diffraction profiles shows good agreement with experimental profiles. In addition, more realistic CF models based on fiber core and thin fiber structure are proposed by removing layers of carbon atoms at random positions of each graphitic sheet along the longitudinal axis. Analysis shows that a fraction of the artificial introduced defects is healed during structural equilibration and the Young's moduli of these models, obtained from axial tensile simulations, are in the experimental range.

© 2020 Published by Elsevier Ltd.

## 1. Introduction

Carbon fibers (CFs) have been developed for more than half a century because of their low density, high elastic moduli, and good thermochemical stability [1]. One powerful property of carbon fibers is that their thermo-physical and mechanical properties span a wide range and can be easily modified for the desired applications [2,3]. Therefore, carbon fiber composites, particularly those with polymeric matrices, have been widely used in, construction, automobile parts, aircraft, space craft, and for sports equipment [4–6]. Carbon fiber composites such as the phenolic-impregnated carbon ablator (PICA) [7], are uses in thermal protection systems in spacecrafts due to their light weight and high temperature resistance.

The processing of CFs requires a series of steps, starting with the spinning of the precursor, such as rayon, pitch or Polyacrylonitrile (PAN), followed by stabilization in air and carbonization in an inert environment, both of which involve complex chemical reactions and physical transformations [1]. The choice of the precursor and processing treatments controls the microstructure of CFs, including crystallite size, alignment of crystallites, pore size distribution and the degree of graphitization, which together largely determine the

density, modulus, strength and thermal conductivity. For instance, improvement of the tensile modulus of PAN-based carbon fiber can be achieved by increasing the alignment of the crystallites through increasing the carbonization temperature, albeit at the expense of the tensile and compressive strength [8].

Since microstructure is crucial to the performance boost of the CFs and their composites, the need to understand the microstructure of CFs is increasing. Previous studies characterized the microstructure of CF by means of X-ray scattering, scanning electron microscopy (SEM) and high-resolution transmission electron microscopy(HTEM) [9–11]. These characterizations reveal many sp<sup>2</sup> sheets in the CFs with the fiber axis imperfectly aligned. Defects and sp<sup>3</sup> amorphous carbon can also accompany the sp<sup>2</sup> graphitic sheets because complete graphitization is almost never possible [12]. The graphitic sheets can be arranged to form radial, random, onionskin, skin-core or hollow porous structures, depending on the precursors and processing methods [13]. The complexity of the CF structures makes it difficult to build computational models for a deeper understanding of the structure and properties, which in turn makes it difficult to improve the performance of CF and their composites.

Atomic-resolution computer simulations, specifically Molecular Dynamics (MD), can capture many of the key properties of the precursors [14,15], as well as the essential, though not all, chemical reactions in the pretreatment and carbonization of the CFs. The

\* Corresponding author.

E-mail address: [sphil@mse.ufl.edu](mailto:sphil@mse.ufl.edu) (S.R. Phillpot).

overall experimental pretreatment and processing times of micron diameter fibers are minutes to hours [16]. While such timescales are far beyond the capabilities and timescale of MD simulations, the fundamental physical and chemical processes take place on timescales of nanoseconds or less, which are accessible by MD simulations. For example, the carbonization mechanism in PAN fiber has been investigated using reactive MD [14]. Indeed, by looking at fibers with thicknesses of a few nanometers, not only are the individual chemical processes present in the larger experimental fibers accessible, but also microstructural changes in the fiber can be characterized, albeit at a small length scale. Recently, atomistic models of CFs beyond simple stacks of graphitic layers have been proposed and have been used to investigate the properties of CFs. Penev et al. [17] probed the atomistic mechanisms of the tensile failure by designing an atomistic model to represent the basic structural units of CFs, which combined curved graphitic sheets and amorphous carbon region. Joshi [18] et al. generated CF models through reactive MD by inserting many ladder units (smaller graphitic fragments, as described in more detail below) at random positions in the simulation box and then inducing their self-organization by compressing and heating the system to create the turbostratic microstructure of fibers. Although the CF structures generated by this method have similar densities and Young's moduli to the experimental values, the densities of the simulated CFs lie in the narrow range from 1.64 to 1.93 g/cm<sup>3</sup> and are essentially prescribed by the compression procedure and the potential. However, the density of experimental CFs range from 1.75 to 2.18 g/cm<sup>3</sup>; some hollow carbon fibers even have densities as low as 0.6–0.8 g/cm<sup>3</sup> [9]. Another very attractive carbon fiber model was proposed by Desai et al. [19], which combined MD and kinetic Monte Carlo (kMC) to generate CF microstructures starting from small ladder-like units, which are similar with the ladder units used by Joshi but simpler. This approach relies on the stochastic cross-linking reactions with constraints applied so that the graphitic sheets align along the fiber axis. Both methods presented by Joshi and Desai show the capability to generate high fidelity CF models at the atomic scale, with overall fiber dimensions of tens of nanometers. However, the generated CF models by each of methods have periodic structures, which make them difficult to combine with other materials, such as a polymer matrix, for a composite model. Simply embedding the periodic CF structure in other materials leads to many physically unexpected dangling bonds near the free surfaces of the CF. One of the key aims of this work is to develop a nonperiodic CF model, which has the potential for modeling composite materials.

The specific objectives of this work are (1) to develop a method to generate non-periodic CFs microstructure with free surfaces based on Desai's model, (2) to characterize the microstructure of periodic CF and non-periodic CF models and compare the differences in density, shape, pore size distribution and virtual X-ray diffraction, and (3) to characterize the tensile strength of these models. Detailed description of the generation and characterization methods are given in Section 2 and the results of the characterization and mechanical deformation are presented in Section 3. Our conclusions are in Section 4.

## 2. Simulation and characterization methods

### 2.1. A brief introduction to kMC-MD model

The kMC-MD model of Desai et al. takes a very thin layer of a large number of identical, vertically aligned multi-carbon fragments, known as ladder units, and allows them to polymerize to form long ribbons of carbon atoms that are irregularly nested in the cross-sectional morphology of a fiber. This is then reproduced along

the axis of the fiber to produce fibers of arbitrary length. The ladder unit is shown in Fig. 1. Each ladder unit consists of eight carbon atoms and is arranged in a hexagonal manner. Such ladder units are capable of forming graphitic ribbons by linking to other ladder units; the ribbon can then be replicated to form the graphitic sheet. To produce a carbon fiber structure, a large numbers of ladder units are packed randomly in the simulation cell with periodic boundary conditions applied in all three directions. The one graphite-ring thick ladder units are perfectly aligned with the longitudinal axis (z-direction) and stand vertically in the x-y plane. The cross-section of the cell (x-y plane) can be varied to produce carbon fiber microstructure with diameters of up to a few tens of nanometers. Specifically, the cross-linking process involves the creation of bonds between the ladder units and is managed by the kMC-MD algorithm developed by Desai et al. This algorithm first identifies unsaturated sp carbon atom pairs in ladder units that are candidates for bond formation, using prescribed cutoff criteria for the distance  $R$  and dihedral angle cutoff  $\theta$ . Bonds are created between a specific fraction  $\eta$  of candidate ladder units chosen at random. Then, the whole system is equilibrated again. The quasi-2D CF microstructure is generated by repeating many cycles of the above steps. Desai also proposed to vary the cutoffs every interval of cycles in the cross-linking process to obtain a more uniform and realistic microstructure as compared to single-cutoff models. In particular, the primary cutoffs in the model: the cutoff capture distance between reactive carbon atom pair  $R_0$ , the cutoff of dihedral angle between two ladder units  $\theta_0$  and the fraction  $\eta_0$  are changed to the secondary values  $R_1$ ,  $\theta_1$  and  $\eta_1$  every three cycles. The detailed procedure and cutoff values of CF generation are introduced in Section 2.2.

### 2.2. CF generation procedure

The ladder units are packed in the simulation cell using the *Packmol* package [20]. In the relaxation of the initial structure and bonds formation process, the simple and computationally efficient Dreiding force field [21] is used to describe the covalent atomic interactions, while the Lennard Jones (LJ) form is used to describe the van der Waals interactions. The *Moltemplate* package [22] is used to attach the Dreiding force field and bonds information to the coordination files. The densities of the initial structures are varied from 1.2 g/cm<sup>3</sup> to 2.0 g/cm<sup>3</sup> by controlling the number of ladders inside the box. The steps in the MD method to generate the CF structure are:

1. Equilibrate the whole system at 300 K for 25 ps with a 0.25 fs timestep at constant volume and temperature, with the temperature controlled using the Nose-Hoover thermostat [23].
2. Run the kMC-MD bond formation cycle as described in Section 2.1 for 360 loops to ensure graphitization of the CF. The key parameters are the primary and secondary capture distances,

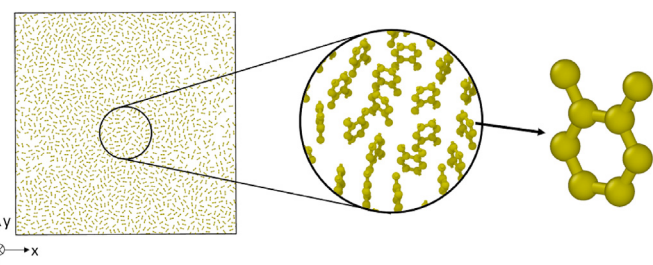


**Fig. 1.** Top view of the initial system packed with ladder structures. A region of the microstructure and a ladder structure are enlarged for clarity. (A colour version of this figure can be viewed online.)

- $R_0 = 5 \text{ \AA}$  and  $R_1 = 2.85 \text{ \AA}$ , the primary and secondary dihedral angle cutoffs  $\theta_0 = 60^\circ$  and  $\theta_1 = 1^\circ$ , the primary and secondary fraction values  $\eta_0 = 0.1$  and  $\eta_1 = 1.0$ . For each loop, a 50 ps NVT equilibration is performed after bond creation.
3. Replicate the quasi-2D microstructure obtained from the graphitization process (step 2) in the z-direction 15 times to generate the 3D microstructure. While the original thickness of the simulation cell was 5.1 Å in the z-direction, after replication it is 76.5 Å; this is the final length of the fiber.
  4. Equilibrate the fiber core with the ReaxFF potential at 300 K for 10 ps with a 0.1 fs timestep and zero pressure. As discussed below, the specific application of the constant pressure algorithm depends on the type of CF structure considered.
  5. Because of its three-dimensionally periodic structure, the microstructure of fiber core is relaxed in all three dimensions. Since the simulation cell of the thin fiber is periodic only along the fiber direction and the fiber sits in a vacuum in the other two directions, zero-pressure control is applied in the axial direction only. This allows the fiber to undergo thermal expansion in all three dimensions.

The LAMMPS software is used for all MD simulations presented in this work [24]. During Step 4, the physically more realistic ReaxFF (reactive force field) [25] is used instead of the less accurate but more computationally efficient Dreiding potential, which is used in generation Steps 1–3. The parameters of the ReaxFF force field are derived from quantum mechanics and provide a more accurate description of atom interactions than the Dreiding potential. Unlike the Dreiding potential, the ReaxFF potential doesn't need to explicitly specify bonds between atoms. It allows dynamic bond breakage and formation by using the concept of bond order within a reactive system. Most importantly, by using the ReaxFF force field, the generated CF model has a wider field of applicability. Particularly relevant for ablative heat shields, ReaxFF can describe the reactions between CF and other chemical species, most specifically both atomic and molecular oxygen. It can also be used to explore the properties of the interface between CF and other materials, such as the phenolic resin, which is a key part of the ablative heat management system.

### 2.3. Controlling the shape of CF

Desai's MD-CF model well describes the cross-sectional microstructure of a carbon fiber. Because of the periodic nature of the simulation cell, the generated graphitic sheets are connected with each other from top to bottom and from left to right. Thus, this periodic structure can be considered to represent a small section of the interior region of a large fiber. We call this microstructure a fiber core.

We are also interested in the surface structure of the fiber and how the fiber interacts with the environment. Thus, we create thin carbon fibers with well-defined surfaces. To prepare such fibers, the ladder units are packed in a cylindrical region in the simulation box. Then, a virtual energy wall is implemented for the relaxation of the initial ladder structure and the graphitization simulation. The specific form of the energy wall is unlikely to be important; the equation defining the energy wall used here has a Lennard-Jones 9–3 form and is given by:

$$E = 4\epsilon \left[ \frac{2}{15} \left( \frac{\sigma}{r} \right)^9 - \left( \frac{\sigma}{r} \right)^3 \right] \quad (1)$$

where  $r$  is the distance from the wall,  $\epsilon = 1.0$  is the strength factor,  $\sigma = 1.0 \text{ \AA}$  is the size factor for wall-particle interaction and the distance cutoff from wall at which wall-particle interaction is 2.5 Å.

The implementation of this virtual force energy wall is achieved by the “fix wall/region” command in LAMMPS. The result is that the fiber is restricted to a cylindrical region at the center of the simulation cells (see Fig. 2). After graphitization, a preliminary microstructure is obtained, with the structural units already being connected by the C–C bonds, after which it is no longer necessary to maintain the virtual energy force wall during the final ReaxFF equilibration in step 4. Although the microstructure continues to undergo localized adjustment, the overall shape of the CF doesn't change even without the constraint of the virtual energy force wall during ReaxFF relaxation. More details will be given in Section 3.

### 2.4. Structural characterization of generated CF

A detailed structural characterization of both the fiber core and thin fiber models is conducted, including the shape and density, an analysis of the carbon hybridization, bond angle distribution function, pore size distribution, and a determination of the expected virtual wide angle X-ray diffraction (WAXD) pattern. The virtual XRD diffraction simulation is conducted using the LAMMPS command “compute xrd” developed by Coleman et al. [26]. The Ovito software [27] and its Python interface are used for visualizing the CF models, monitoring the volume change, and characterizing the carbon hybridization of CFs. Unlike the dense fiber core, one third to one-half of the volume of the simulation cell of the thin fiber is open volume, external to the fiber surface. This enables the thin fiber to develop a three-dimensional irregular shape during the ReaxFF equilibration in generation step 4. The surface irregularity makes the calculation of the volume of the fiber more difficult; thus, to accurately compute the volume of thin fiber, the “Construct Surface Mesh” modifier of Ovito is used to construct a polyhedral surface mesh around the carbon atoms (see Fig. 3); the actual volume of the fiber is then determined from the enclosed area. To construct a surface mesh, a virtual probe sphere is used to identify the accessible open region where the sphere does not touch any atom. In this work the radius of the virtual probe sphere to identify the open area is chosen to be 12 Å; this avoids counting small internal cavities or pores inside CF as open regions. A pore size distribution (PSD) calculation code [28], suitable for the thin and fiber core model was developed, building on the code of Joshi et al. [29], in which the pore size is defined as the maximum distance between two point within the pore. However, our code also filters out the open area outside the thin fiber, thereby capturing the internal porosity. In addition, the efficiency is also improved by replacing the for loops with graph networks [30] using the Boost graph library [31] during the atom bins connectivity check.

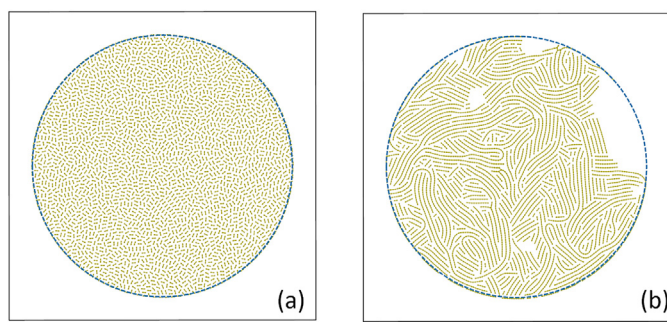


**Fig. 2.** (a) The top view of a well-relaxed initial structure after NVT relaxation (Step 1); (b) The graphitized structure of thin fiber obtained after bond formation (Step 2), where the virtual energy force wall is represented as a blue dashed cycle.

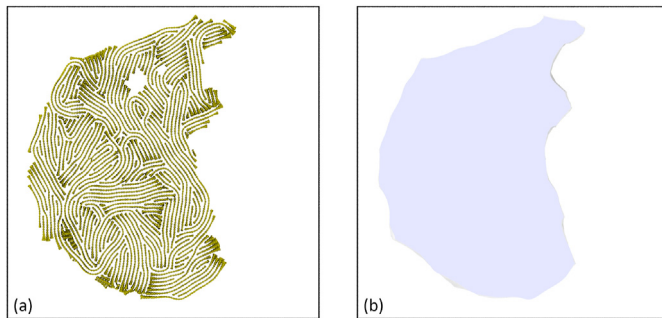


**Fig. 3.** (a) Top view of the thin fiber where carbon atoms are colored as gold (b) Top view of the surface mesh of the same fiber model. (A colour version of this figure can be viewed online.)

## 2.5. Discontinuous CF model

In the idealized model considered to this point, the graphitic sheets are continuous along the longitudinal direction of the fiber, having neither breaks nor imperfections; by contrast, in a real fiber, these sheets are of a finite length and have defects of various types such as discontinuities (i.e. breaks) in the graphitic sheets, nanopores and amorphous regions [32,33]. Because it is hard to break covalent C–C bonds, it is extremely difficult to break a continuous CF model in tensile tests. By contrast, a real fiber has graphitic sheets of finite length. In addition, the carbon fibers are not perfectly aligned graphitic sheets and the axes of long graphitic sheets can deviate from the fiber axis by 15–25° [34]. Voids and nanopores can also exist in the real fiber; their concentration and precise nature depend on the type of precursor and the degree of carbonization. Indeed, the tensile strength of a real fiber is much less controlled by the breaking of covalent bonds than by these defects.

In order to represent the effect of the defects in carbon fibers along the longitudinal direction, each graphitic sheet is severed into two pieces at a random position in the z-direction by removing an entire plane of carbon atoms. In this way, the tensile strength is controlled by both covalent bond and the weak van der Waals interactions between the sheets rather than by breaking the covalent bonds, which is very difficult. The computational process to introduce these breaks is complicated by the morphology of the fiber. In particular, as illustrated in Fig. 4 (a) and 4(b), a single sheet can involve a number of branches joined by  $\text{sp}^3$ -bonded carbon atoms. To mimic the finite length of the graphitic sheets along the fiber direction, one plane of carbon atoms is removed at a random z-position, as shown in Fig. 4(c), in which the removed carbon atoms are shown in red. The closest planes of atoms above and below the defect are labeled in blue and green in Fig. 4(c). Fig. 4(d) shows a 3D view of the fiber core, in which gaps between the graphitic sheets are colored in red. After removing these planes of atoms, the whole system is relaxed with constant temperature and pressure (NPT) at 300 K for 10 ps before the tensile simulation. In the tensile test, all samples in this work are stretched along fiber axis (the z-direction) at a strain rate  $10^{10} \text{ sec}^{-1}$ , a typical strain rate for computational tensile tests [35,36]. Because the thin fiber is embedded in vacuum, the pressure on thin fiber is calculated as the ratio between pulling force and the cross-section area of the fiber, which is the area of cap identified by the surface mesh method (see Fig. 3(b)). The relaxation and tensile simulation are performed using the ReaxFF potential.

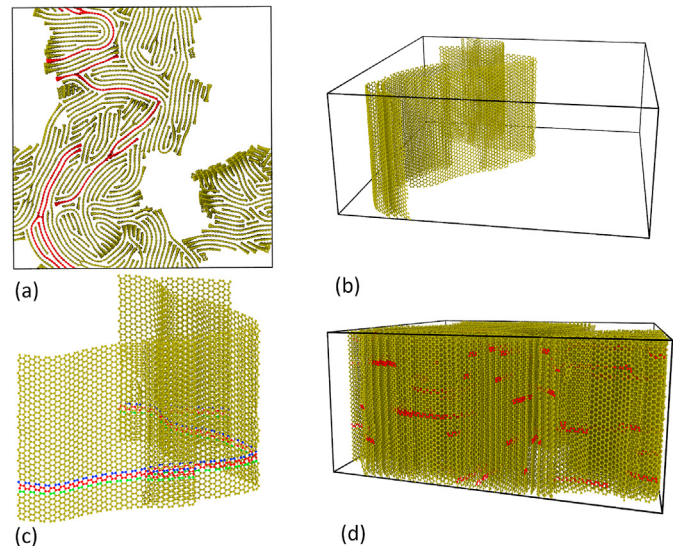


**Fig. 4.** (a) The top view of core fiber where two graphitic sheets are selected and colored as red; (b) The 3D view of two graphitic sheets which are selected in (a); (c) The 3D view of one graphitic sheet where red carbon atoms will be removed, blue carbon atoms are the top margin of the defect and green carbon atoms are the bottom margin (d) The 3D view of the core fiber and the artificial introduced defects, which will be removed, are colored as red. (A colour version of this figure can be viewed online.)

## 3. Microstructure of CF

### 3.1. Initial configurations and snapshots of CF models

It is anticipated that the density and shape of the fiber will be the key characteristics that will affect their mechanical properties; these are investigated in this work. The configurations for the initial system, as well as other model characteristics such as the system size and number of atoms, are given in Table 1. For the fiber core, the volume used for calculating the initial density is that of the simulation box. For the thin fiber, the volume for labeling the initial density is defined as the volume enclosed by the virtual force wall, which is used to produce the fiber. Of course, as will be discussed below and as can be seen in Fig. 5, the actual physical densities of the thin fibers are more similar to graphite.

Fig. 5 shows snapshots taken from structures for both fiber cores and thin fibers after bond formation and ReaxFF relaxation for various densities. The simulation cells for the fiber cores shrink after NPT relaxation; therefore, the actual size of the corresponding systems after NPT relaxation is slightly smaller than these after bond formation cycles although these pictures shown in Fig. 5 have same size for tidiness and clarity. The snapshots of the fibers show that, with increasing initial density, the initial structure of both the fiber core and the thin fiber have more uniform structures and fewer and smaller pores. Comparing the microstructures generated after bond formation, both corresponding core fiber and thin fiber samples keep approximately the structure periodicity along the z axis and have similar shapes after ReaxFF relaxations.

### 3.2. Shapes, densities and pores

An important structural feature that influences CF properties is the presence of pores inside the fiber. Therefore, in this section we analyze the final density, the size and distribution of pores, and the shape of the CFs.

**Table 1**

Densities, number of atoms and system size of the initial system used in the generation of CFs as well as the corresponding CF type. For each core fiber, the initial system size is characterized by the length of the simulation box at x, y, z three dimensions. For each thin fiber, the initial system size is characterized by the diameter of circular virtual force wall and the height of the simulation box.

Initial density (g/cm <sup>3</sup> )	Number of atoms	Initial system size (Å)	Carbon fiber shape
1.2	12272	200 × 200 × 5.1	Fiber core
1.4	14320	200 × 200 × 5.1	Fiber core
1.6	16368	200 × 200 × 5.1	Fiber core
1.8	18408	200 × 200 × 5.1	Fiber core
1.9	19432	200 × 200 × 5.1	Fiber core
2.0	19640	200 × 200 × 5.1	Fiber core
1.2	13880	240 × 5.1	Thin fiber
1.4	16200	240 × 5.1	Thin fiber
1.6	18512	240 × 5.1	Thin fiber
1.8	20824	240 × 5.1	Thin fiber
1.9	21984	240 × 5.1	Thin fiber
2.0	22208	240 × 5.1	Thin fiber

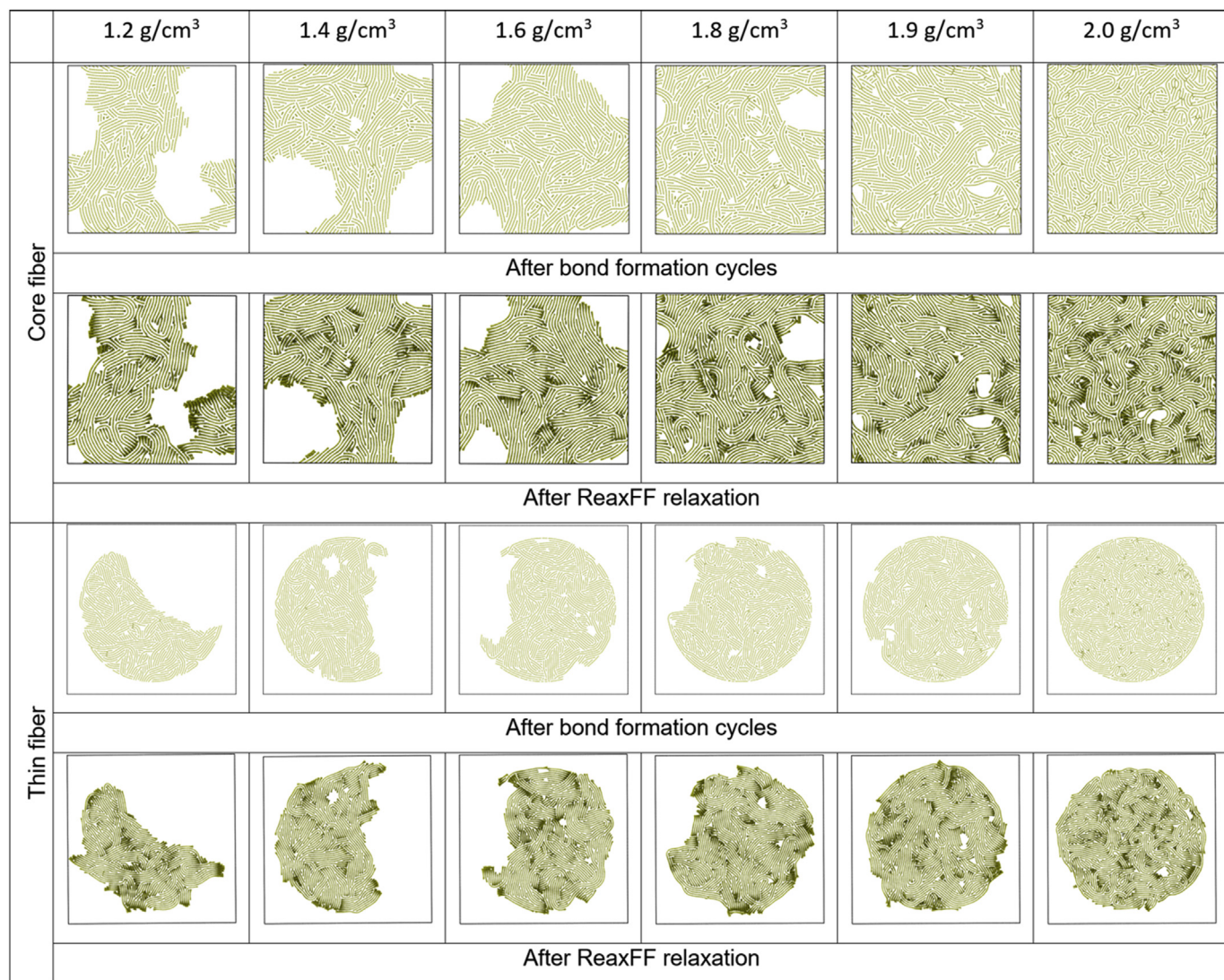


**Fig. 5.** Atomistic snapshots of fiber core and thin fiber microstructures after bond formation cycles and ReaxFF relaxation with various initial densities from 1.2 g/cm<sup>3</sup> to 2.0 g/cm<sup>3</sup>. All snapshots are top views of CF microstructures and all carbon atoms are colored as green. (A colour version of this figure can be viewed online.)

**Fig. 6** compares the initial and final densities of fiber cores and thin fibers. As shown in **Fig. 6**, all fiber core and thin fiber structures lie above the green dash line, indicating that they are all densified after the generation process. The final structures of the fiber cores

are denser by 0.1–0.2 g/cm<sup>3</sup> after the generation process. By contrast, all of the thin fibers have essentially the same final densities (in the range 2.16–2.19 g/cm<sup>3</sup>) after step 4. Some of the fiber cores have final densities in the experimental range of 1.75–2.0 g/

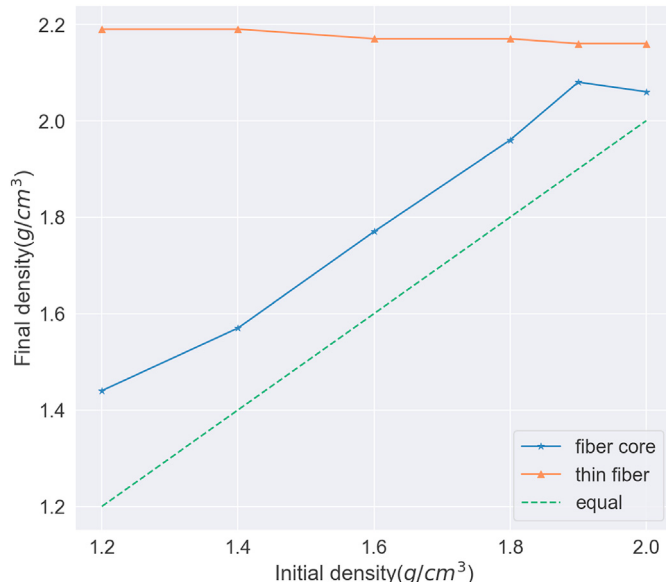


**Fig. 6.** The initial and final densities of fiber core and thin fibers after NPT relaxation with ReaxFF potential. The green dash line indicates the structure of same initial and final density. (A colour version of this figure can be viewed online.)

cm<sup>3</sup> for PAN fibers [34], while others are lower. However, thin fiber models have similar final density regardless of the initial densities. These values are similar to the density range of 1.9–2.2 g/cm<sup>3</sup> of pitch-based carbon fiber [16] and close to graphite's density of 2.236 g/cm<sup>3</sup> [34].

Fig. 7 shows the pore size distributions for the fiber core and thin fiber for various initial densities respectively. As shown in Fig. 7, the fiber cores have slightly smaller pores after NPT relaxation. The shape of thin fiber also changes during this relaxation. Thin fibers contain a few large pores before NPT relaxation. However, after NPT relaxation, all the thin fibers have similar pore size distributions, independent of the initial density and initial pore size distribution: the average pore size is 4 nm, with various volume fractions, which indicates that pores shrank and that some were healed during the relaxation. The similar pore size distributions and final densities also indicate that these thin fibers have similar microstructures, even though they have different initial densities and shapes of final structures.

Fig. 8 shows the total volume fractions of pores in fiber cores and thin fibers for various initial densities. The final volume fraction of pores decreases in the fiber cores with increasing density of the initial structure, while it is independent of the initial density in the thin fibers. More interestingly, with increasing initial density, the volume fractions of pores in the fiber core gradually decrease to the same level as in the thin fiber. The total volume fraction of pores decreases for both fiber core and thin fiber structures after NPT relaxation. Since most of pores close up in the thin fiber after NPT relaxation, we conclude that the initial density of the thin fiber model doesn't influence the distribution of pores, but only the shape of final structures and that the density of a fiber region without pores in this model is around 2.2 g/cm<sup>3</sup>. Moreover, the difference of the pore size distributions of the thin fiber and fiber core shows that the pores stay in the fiber core but heal up in thin fiber after NPT relaxation because of the free surface.

### 3.3. Hybridization state of carbon

One important characterization of the carbon fiber model is the carbon hybridization. Fig. 9 shows the evolution of the carbon

hybridization during bond formation and NPT relaxation of fiber cores for various initial densities. Because the thin fiber microstructures and the fiber cores undergo similar evolutions, here we only show and analyze the hybridization changes for fiber core samples. Beginning with the initial structures described in Section 3.1, the unsaturated sp hybridized carbon atoms from different ladder units bonded with each other and gradually became sp<sup>2</sup>, or in a few cases sp<sup>3</sup>, hybridized. The sharp decrease of sp population and increase of sp<sup>2</sup> population in Fig. 9(a–b) show that most of reactive sp carbon atoms link with each other in the first 500ps, especially for high initial density structures such as 1.9 and 2.0 g/cm<sup>3</sup>. For high initial density structures, the average distance between unsaturated carbon atoms is smaller, which results in the distance cutoff requirement being easier to meet. Therefore, the slopes of sp and sp<sup>2</sup> population at initial stage of bond formation are steeper for high initial density structures. The higher initial density also results in the ladder units not having enough space to adjust their position during the graphitization process, which lowers the probability of bond creation. For these two reasons, the 2.0 g/cm<sup>3</sup> sample has a very sharp increase in the number of sp<sup>2</sup> bonds at the beginning of the bond formation. Compared with microstructures of other initial densities, both fiber core and thin fiber structures at 2.0 g/cm<sup>3</sup> shows a uniform, almost pore-free microstructure, as shown in Fig. 5. This is a result of the ladder unit having little space in which to reorient, resulting in a lower population of sp<sup>2</sup> hybridization after bond formation. Except for the 2.0 g/cm<sup>3</sup> initial structure, which has a relatively higher sp population, all other structures reach similar sp and sp<sup>2</sup> populations after bond formation. Fig. 9(c–d) show the sp and sp<sup>2</sup> population change during NPT relaxations for fiber cores of various densities. Since the bond creation is explicitly managed by the kMC-MD algorithm, there is no sp<sup>3</sup> population generated during the graphitization process.

The ReaxFF potential enables the automatic breaking and creation of bonds during the simulation; therefore, the self-organization and reactive fusing of carbon atoms still happens during this stage. The hybridization profile under NPT condition shows carbon atoms keep bonding with other atoms and forming more sp<sup>2</sup> C–C bonds. Compared with the hybridization evolution during bond formation in Fig. 10(a–b), the change of hybridization is smaller under NPT relaxation, indicating that most of sp<sup>2</sup> carbon atoms formed in the bond formation process. As Fig. 10(c–d) show, the sp content rapidly decreases and sp<sup>2</sup> content increases in the first 5ps during NPT relaxation, with the hybridization converging gradually. The sp<sup>2</sup> content increases during ReaxFF relaxation by 2–3% for both fiber core and thin fiber models. Also, a few sp<sup>3</sup> hybridized carbon atoms are detected at the branching position of the graphitic sheets during ReaxFF relaxations. All samples, other than the 2.0 g/cm<sup>3</sup> sample, have similar sp<sup>3</sup> hybridization percentages: about 0.03%. The sp<sup>3</sup> concentration in the 2.0 g/cm<sup>3</sup> sample is 0.1%, which is still a very small amount compared with the concentration of sp and sp<sup>2</sup>. As discussed above, the high initial density of these samples prevents the microstructure from evolving due to minimal amount of space available for ladder units to adjust their positions. Low initial density also makes the distance between unsaturated carbon atoms larger than the cutoff and decreases the percentage of sp<sup>2</sup> bonds formed. As a result, the sp<sup>2</sup> hybridization reaches a maximum for an initial density of 1.6 g/cm<sup>3</sup>.

### 3.4. XRD analysis

The structures of the simulated carbon fiber models can be analyzed through their XRD patterns; this also enables a direct comparison of key microstructural features, such as interplanar spacing, with experimental results. Again, we only analyze the XRD

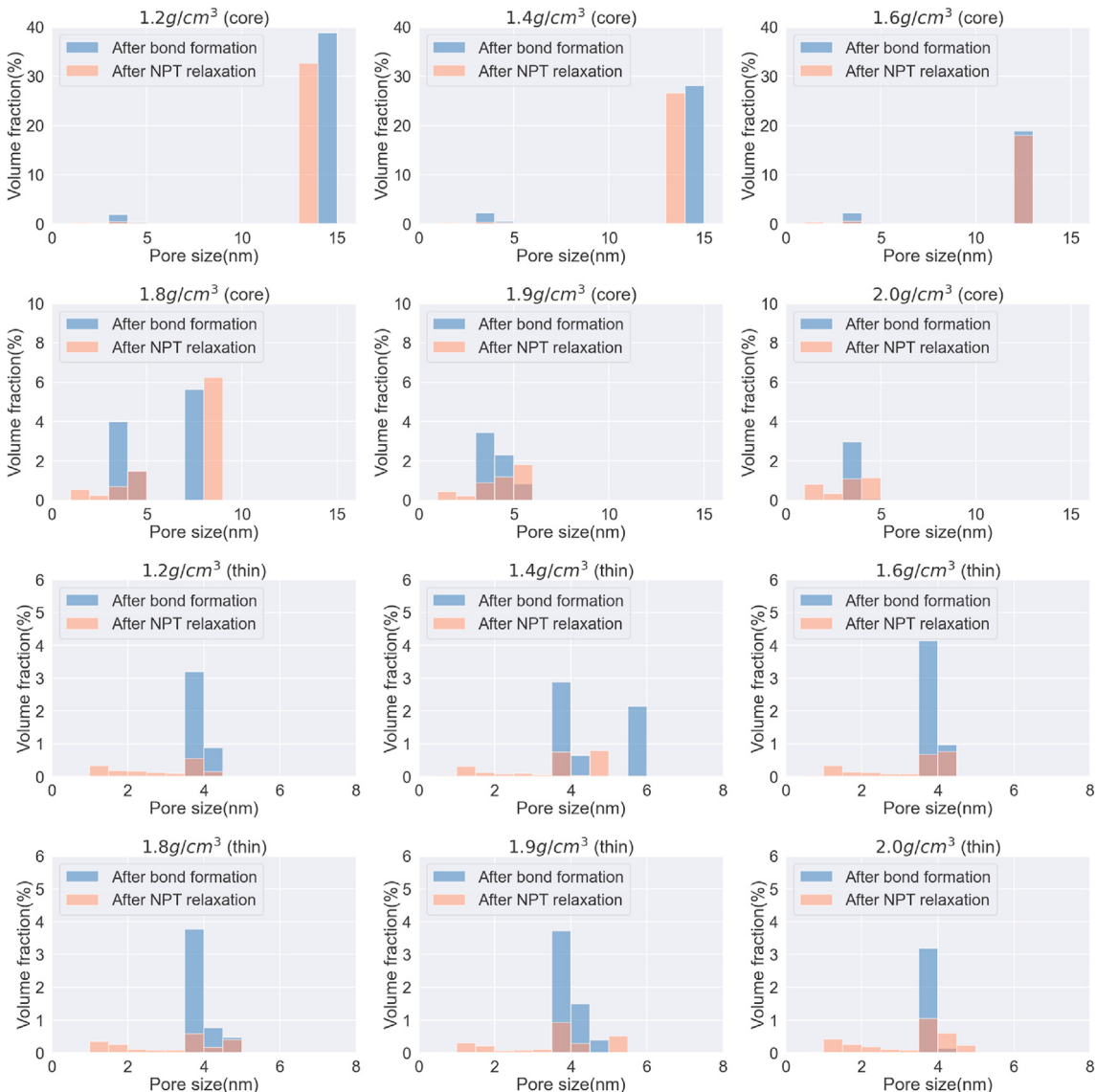


**Fig. 7.** Pore size distribution of fiber cores and thin fibers for various initial densities ranging from 1.2 to 2.0  $\text{g}/\text{cm}^3$  (PSDs for structure after bond formation and NPT relaxations are colored as blue and orange respectively). (A colour version of this figure can be viewed online.)

patterns of the fiber core because the thin fiber models show similar behavior. The indexing notation we used in Fig. 11 follows that in Ref. [37], in which the (100) planes are stacked in the zigzag direction and the (110) planes are stacked in the armchair direction of the basal planes of the graphitic sheets.

Fig. 10(a) shows the calculated virtual XRD profile of fiber core structures of various initial densities, which are presented as stacked curves for clearer representation. All structures, regardless of initial density, have peaks of almost the same intensities at identical positions, except the 2.0  $\text{g}/\text{cm}^3$  structure which has a slightly broad and less intense peak at  $2\theta = 27^\circ$ . Fig. 10(a) thus shows that the initial density doesn't have a strong influence on the structure. Fig. 10(b) shows the XRD patterns taken from the 1.2  $\text{g}/\text{cm}^3$  core fiber model before and after NPT relaxations. The first peak occurs near  $2\theta = 27^\circ$  and corresponds to the interplanar spacing ( $d_{002}$ ) in graphite and can be attributed to the graphitic region in the carbon fiber. According to Bragg's equation, the interlayer spacing  $d_{002}$  value is 0.33 nm. The previous XRD measurements performed on PAN-based

carbon fibers with various heat treatment temperatures have reported  $d_{002}$  spacings ranging from 0.344 nm to 0.351 nm [38]. The peaks at  $\sim 42.5^\circ$  and  $57.6^\circ$  correspond to the (100) and (004) planes respectively. These two peaks have also been observed in the previous PAN-based carbon fibers experiments [38]. However, the X-ray diffraction pattern obtained from the experiments shows a relatively weaker (100) peak compared with the peak in these virtual X-ray diffraction patterns. This can be attributed to the higher crystallinity in our fiber model. The peaks at  $\sim 74.5^\circ$  and  $76^\circ$  correspond to the (110) plane in the fiber core before and after NPT relaxation, respectively. Because the (110) plane is parallel to the x-y plane in our model and the number of layers of (110) planes is fixed, this peak not only characterizes the interplanar spacing of (110) planes but also reflects the change in the length of the simulation box along the z direction. The (110) peak is at a higher angle after NPT relaxation, indicating a smaller interlayer spacing  $d_{110}$  than the structure before relaxation. This is consistent with the box length shrinkage from  $\sim 76.5 \text{ \AA}$  to  $\sim 75.2 \text{ \AA}$  for the fiber core structure.

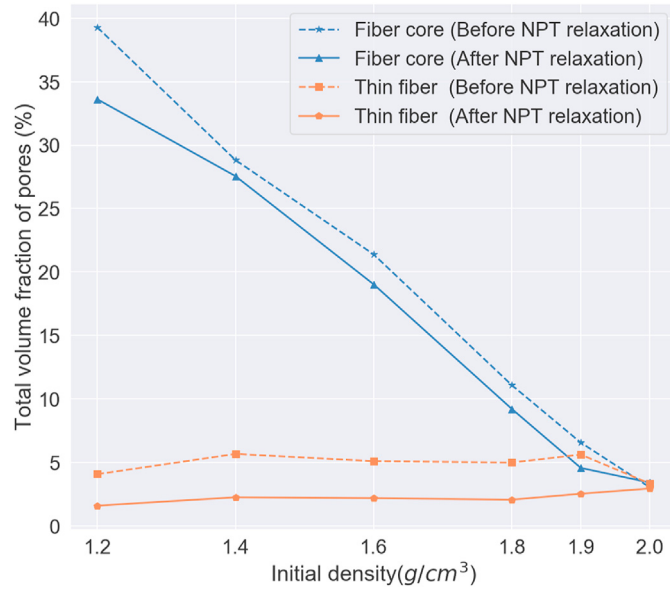


**Fig. 8.** Total volume fraction of pores of fiber microstructures for various initial densities ranging from 1.2 to 2.0 g/cm<sup>3</sup> after bond formation (dash lines) and NPT relaxations (solid lines). (A colour version of this figure can be viewed online.)

Both the highly ordered graphitic sheets shown in the atomistic snapshots in Fig. 5 and the sharp XRD peaks in Fig. 10 result directly from the presence of graphitic crystallites in the fiber core and thin fiber models. The average size of these crystallites can be estimated from the X-ray diffraction pattern using Scherrer equation:

$$L(hkl) = \frac{K\lambda}{B(2\theta) \cdot \cos\theta} \quad (2)$$

where  $\lambda = 0.154$  nm is the wavelength of the X-rays,  $\theta$  is the diffraction peak  $B(2\theta)$  of the  $(hkl)$  plane,  $B(2\theta)$  is the full width at the half maximum (FWHM) of the diffraction peak and  $K$  is shape factor which varies with the type of crystal structure. Two values are often used to describe the size of microstructure. The crystallite thickness ( $L_c$ ), which is the average size perpendicular to the graphitic sheets, is calculated from the (002) diffraction peak. The crystallite correlation length ( $L_a$ ) along graphitic sheets can be subdivided into  $L_{a\parallel}$  parallel with the fiber axis and  $L_{a\perp}$  perpendicular to the fiber axis.  $L_{a\parallel}$  and  $L_{a\perp}$  are associated with (100) and (110) planes, respectively, and can be determined from the corresponding peaks in the diffraction pattern. The shape factor  $K$  is 0.89 and 1.84 for  $L_c$  and  $L_a$ , respectively [39]. Since the graphitic sheets in CF models are highly aligned along the fiber axis, the  $L_{a\parallel}$  of CF models are determined by the length of the simulation cell.

Previous experimental studies [39–41] have reported the  $L_c$  for PAN-based carbon fiber varies in the range 1.6–7.8 nm. Although the experimental values of  $L_c$  vary widely because of the different processing treatments, as shown in Table 2, the values thus obtained for both fiber core and thin fiber structures after NPT relaxation show that the generated microstructures have relatively small and similar crystallite size and correlation length, which lie within the range of the experimental values. Both fiber core and thin fiber shows a lower  $L_c$  value for microstructures of 2.0 g/cm<sup>3</sup> initial density compared with samples of other initial densities. Similar to the analysis in Section 3.3, the high initial density hampered the combination and growth of graphite crystallites, which caused the low average graphite crystallite size compared

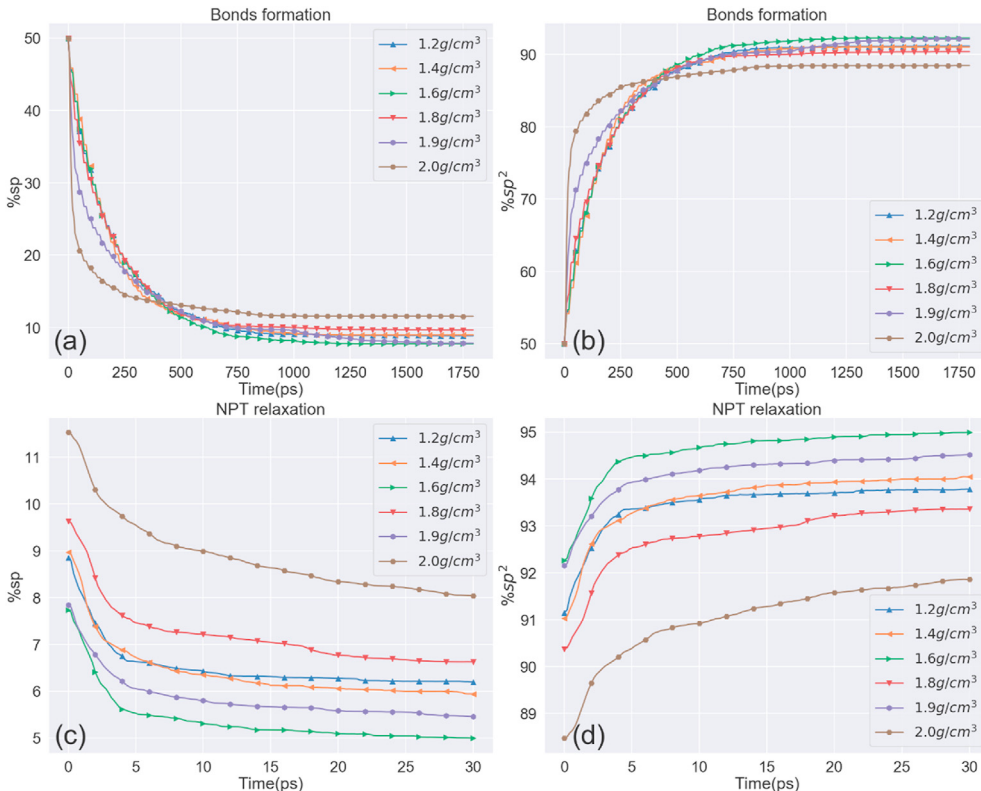


**Fig. 9.** Evolution of carbon sp and sp<sup>2</sup> hybridization content for fiber cores with various initial densities during (a, b) bond formation and (c, d) NPT relaxation. Thin fiber structures show similar trends. (A colour version of this figure can be viewed online.)

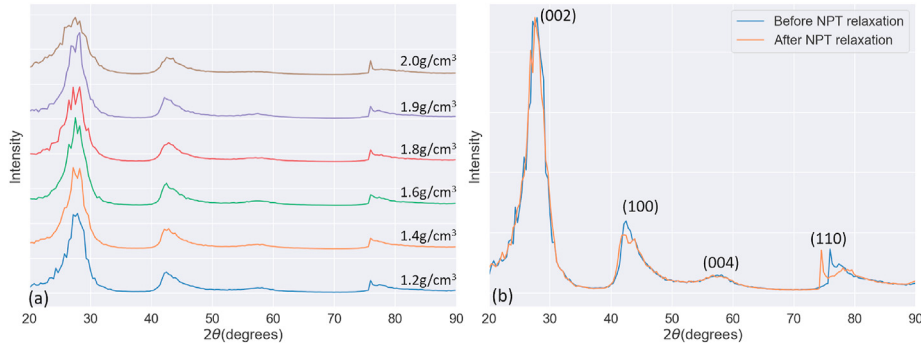


**Fig. 10.** (a) Simulated virtual XRD pattern from the core fiber model of different densities ( $1.2\text{ g}/\text{cm}^3$ - $2.0\text{ g}/\text{cm}^3$ ) (b) The XRD profile comparison of  $1.2\text{ g}/\text{cm}^3$  core fiber structure before and after NPT relaxation. Similar trends have been observed for the thin fiber model.

with low initial-density microstructures. The obtained  $L_{a\perp}$  value is ~13–16 nm using Scherrer equation, which is higher than the experimental value, ranging from 5 to 8.4 nm [41]. Similarly, an  $L_{a\perp}$  value of ~16 nm is also reported in Desai's simulation. This overestimation of  $L_{a\perp}$  can be attributed to the perfect alignment of fibers along the fiber axis in the model. In a real carbon fiber, the long chains are not straight and deviate from the fiber axis. The higher random crosslinking probability between chains in experiments can also prevent the formation of long graphitic sheets. Overall, we conclude that the generated microstructures have similar diffraction patterns that are similar in many respects to those of PAN-based CFs. Moreover, the fiber core and thin fiber have the similar diffraction patterns, indicating that the shape does not influence

the characteristics of the generated microstructures. The shift of (110) peaks in the XRD profiles shows the decrease of interplane spacing of (110) plane after NPT relaxation.

### 3.5. Mechanical properties

In this section, we investigate the mechanical behavior of the CF using the discontinuous CF model. Of course, this CF model is still much simpler than real CFs. Previous study shows that the high strength PAN-based fiber is composed of carbon micro crystallites [42]. These turbostratic graphitic crystallites are poorly oriented but lie preferentially parallel to the fiber axis. The simulated crystallites of models are still highly parallel to the fiber axis. Moreover,

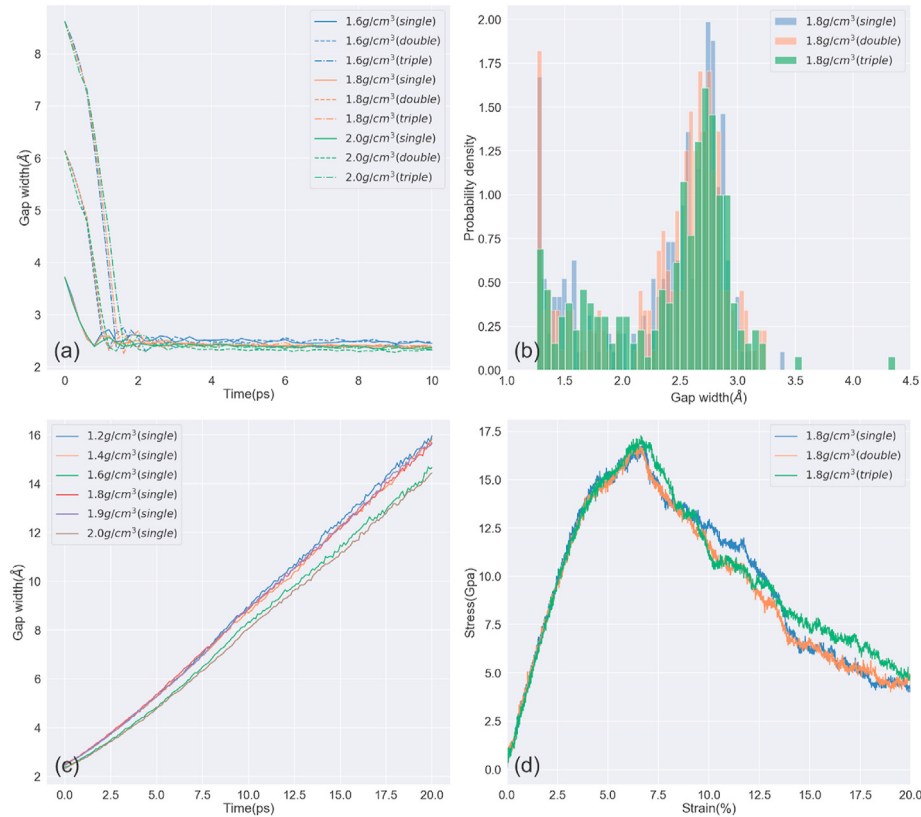


**Fig. 11.** (a) The width change of the artificially introduced break during healing process (b) The width distribution of breaks of different initial width for  $1.8\text{ g}/\text{cm}^3$  fiber core after healing process (c) The width change of the breaks during tensile simulation for fiber core structures with different initial densities ranging from  $1.2\text{ g}/\text{cm}^3$  to  $2.0\text{ g}/\text{cm}^3$  (d) Stress-strain curve of  $1.8\text{ g}/\text{cm}^3$  fiber core with breaks of different initial width. (A colour version of this figure can be viewed online.)

**Table 2**

Average crystallite size of fiber cores and thin fibers for various initial densities.

Initial density(g/cm <sup>3</sup> )	1.2	1.4	1.6	1.8	1.9	2.0
$L_c(\text{nm})$ (Fiber core)	2.29	2.16	2.45	2.84	2.26	1.55
$L_c(\text{nm})$ (Thin fiber)	2.09	2.56	2.35	2.13	2.06	1.67

crystallites in realistic fibers can twist, interweave, and fold with other crystallites, and are accompanied by dislocations, micro voids and amorphous non graphitic carbon regions [43,44]. XRD and Raman spectroscopy reported that amorphous region exist in the in CF, in which carbon atoms mainly have  $\text{sp}^2$  hybridization state and form cross-linked, non-aligned sheets [45]. Using the Mori-Tanaka's mean stress method, Ishikawa et al. reported that the torsional modulus is impacted by the volume of the amorphous [46,47]. Thus, a realistic carbon fiber is much more complicated and much more disordered than the simulated models. Due to the nature of the simulation method, and the replication along the fiber direction, there are no misoriented graphitic sheets along the z-direction. The graphitic region is characterized using the criteria proposed by Joshi [18]: (1) The energy of a carbon atom is ~30 meV/atom, and (2) the carbon atoms are in the  $\text{sp}^2$  hybridization state. We find only few carbon atoms at the edge of the graphite sheet that do not meet this criterion; these have high energy due to their undercoordination. Since all of these microstructural defects and amorphous regions in CF are likely to reduce the mechanical integrity of the experimental systems, the current CF models can be expected to be stronger than real CFs. Therefore, one line of carbon atoms is removed at a random position in each graphitic sheet in the discontinuous model to mimic the presence of defects along the fiber axis. However, this is offset by the very short lengths of the graphitic sheets in the computational models, 76.5 Å, which is substantially less than the experimental values at order of micrometers [48], and likely to make the computational models much more susceptible to the pullout mechanism, described below, than their experimental counterparts.

We observed that some of the artificial breaks in the model graphitic sheets heal during the structural equilibration: this increases the mechanical integrity of the system. In order to quantify the healing of the broken sheets, we tracked the change of the average width of the breaks between the upper and lower parts of what was originally a single sheet. To investigate the influence of the break width, we removed one, two or three layers of carbon atoms in each sheet. Interestingly, we found the fiber model is independent of the width of breaks: as shown in Fig. 11(a), the breaks healed to the same average width. Although wider breaks need more time to heal, all sample healed within 2 ps and the structure remained stable throughout the rest of the simulation. Moreover, it showed that there are still some after re-healing, although the gap width is substantially lowered, and partial breaks disappear. Fig. 11(b) shows the width distribution of breaks of different initial width for 1.8 g/cm<sup>3</sup> fiber core after the healing processes. Since three distributions show similar patterns, it is evident that the initial width has a weak influence on the final width distribution. No matter what the initial width of the breaks are, the breaks partially heal to same final widths, which corresponds well with the finding in Fig. 11(a) that the average break width is nearly independent to the initial width after re-healing. Moreover, Fig. 11(b) shows some gaps are healed and have width less than 1.8 Å, the bond cutoff in the ReaxFF potential, indicating that some covalent bonds are recreated between carbon atoms at the edge of the gap. Therefore, in the tensile simulation, bond breaking still determines the tensile strength but is greatly weakened by the relatively low density of such strong bonds. Fig. 11(c) shows that the break width

increases linearly with tensile strain, which can be attributed to the linear deformation of the simulation cell as function of time in the loading process. Fig. 11(d) shows the stress-strain curves of 1.8 g/cm<sup>3</sup> fiber core models with different initial break widths. Since the average break width is almost same after the re-healing process, samples should have similar defects features. The three almost identical and overlapped stress-strain curve demonstrate that the three samples do indeed share same the defect characteristics.

Fig. 12 shows the stress-strain curves obtained from tensile simulations for the continuous and discontinuous CF samples. The tensile moduli extracted from stress-strain curves are shown Table 3. Fig. 12(a, c) show the simulated tensile moduli of both fiber core and thin fiber are much higher than the experimental value of real CF. A previous study [1] showed commercially available PAN-based CFs have tensile moduli ranging from 230 to 588 GPa with tensile strength ranging from 3 to 7 GPa. Also, the pitch-based CFs have a wider range of tensile modulus from tens up to about one thousand GPa, with tensile strength values from 1 to 4 GPa. As shown in Table 3, the continuous CF samples exhibit extreme high tensile moduli 920–1200 GPa and 1210–1275 GPa for the fiber core and thin fiber respectively. These figures also show that their tensile strengths are approximately five to ten times higher than the real carbon fibers. As Fig. 12(b, d) show, the tensile modulus decreases to levels comparable to experimental level values when the breaks are introduced into the fiber core and thin fiber models. As shown in Table 3, the tensile moduli range from 244 to 413 GPa for discontinuous fiber cores and from 309 to 376 GPa for discontinuous thin fibers. The insets in Fig. 12(a, c) show that the carbon rings begin to break at the yield point in continuous fibers, while the gap width increases in the discontinuous fibers as shown in Fig. 12(b, d). By introducing the breaks in the CF, the tensile strength is reduced and can be attributed to the greatly reduced number of covalent bonds that must be broken; this reduction is partially offset the need to overcome the weak van der Waals interactions as the graphitic sheets slide over each other.

The modulus increases with increasing initial density for both the continuous and discontinuous fiber models. Both continuous and discontinuous thin fiber models have similar moduli nearly independent of the initial density. The thin fiber models have similar moduli with the fiber cores of 1.9–2.0 g/cm<sup>3</sup>. As shown in Figs. 6 and 8, the final density and the total volume fraction of pores of fiber cores approach the values in the thin fibers with increasing initial density, indicating similar microstructures in the high-density thin fibers and fiber cores. Moreover, unlike the fiber core, the thin fiber is non-periodic at x-y plane. Because the graphitic sheets at the outer surface of the thin fiber only interact with one side of other graphitic sheets via van der Waals force, pullout of these fibers is easier than in the interior [49]. Due to the periodic conditions, all the graphitic sheets in fiber core interact with two sides of other sheets via van der Waals interactions, which makes the system stronger. Therefore, although thin fibers have similar densities as the fiber core, the tensile modulus is still slightly lower. It is worth noting that the tensile strength of the discontinuous carbon fiber model is still 2–5 times larger than the experimental value. As discussed at the beginning of this section, the strength of real fibers is further reduced by the misorientation, defects, amorphous regions and micro-voids along the longitudinal direction, which are not captured in this model. Moreover, the high level of alignment along the axis in our fiber model increases the tensile strength.

The transverse moduli of CFs are also computed by conducting tensile simulations in direction normal to the fiber direction. Since there is empty space surrounding the thin fiber, we only compute the transverse modulus of fiber core model. The transverse modulus of CFs has been experimentally evaluated by tensile

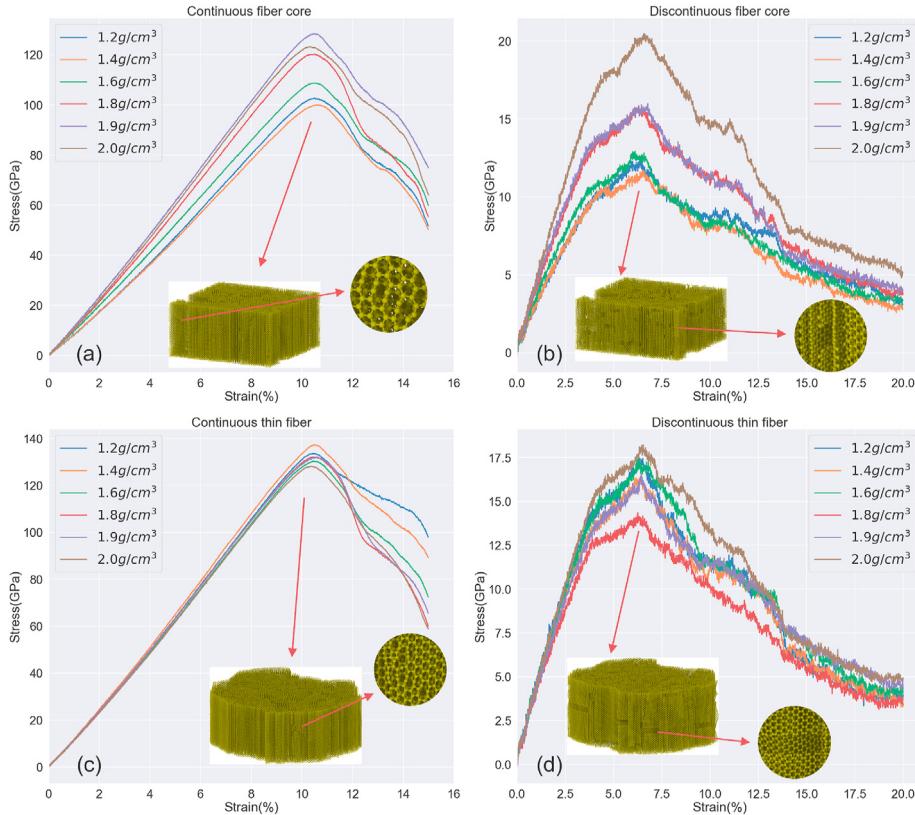


**Fig. 12.** Stress-strain curves predicted in tensile simulation of CF sample for various initial densities and the snapshots of  $1.8 \text{ g}/\text{cm}^3$  samples at yield points. (a) Continuous fiber core samples (b) Discontinuous fiber core samples (c) Continuous thin fiber samples (d) Discontinuous thin fiber samples. (A colour version of this figure can be viewed online.)

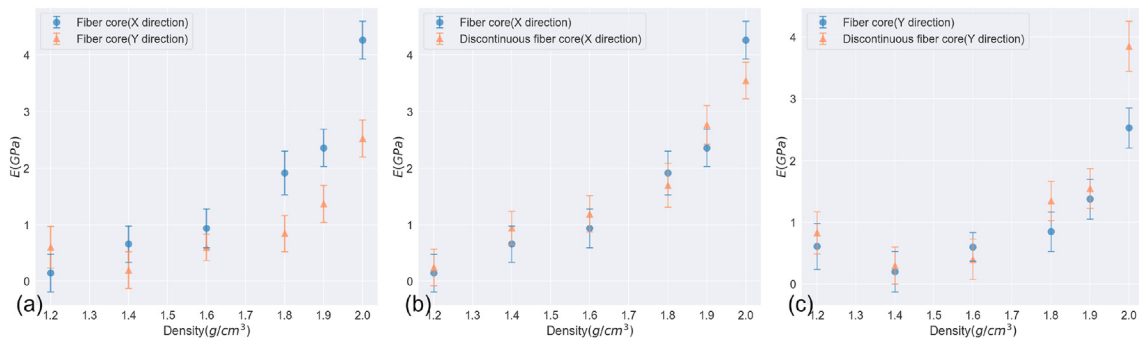


**Fig. 13.** (a) The transverse moduli at X and Y direction of fiber core of different densities ranging from  $1.2$  to  $2.0 \text{ g}/\text{cm}^3$  (b–c) The transverse moduli at X direction and Y direction of continuous and discontinuous fiber cores of different densities ranging from  $1.2$  to  $2.0 \text{ g}/\text{cm}^3$ .

**Table 3**

The tensile moduli of continuous and discontinuous fiber core and thin fibers predicted from the tensile simulation. The corresponding strain-stress curves are shown in Fig. 13.

Initial density( $\text{g}/\text{cm}^3$ )	Fiber core		Thin fiber	
	Continuous (GPa)	Discontinuous (GPa)	Continuous (GPa)	Discontinuous (GPa)
1.2	923	244	1251	356
1.4	911	241	1275	334
1.6	1028	264	1229	353
1.8	1128	328	1246	309
1.9	1211	335	1242	333
2.0	1177	413	1210	376

compression tests [50], showing that the transverse moduli of pitch based and PAN based CFs range from 1 to 4 GPa, while the moduli of some high strength PAN based CFs can be up to 9 GPa. Fig. 13(a)

shows that the transverse moduli of fiber cores range from 0.2 GPa to 4.5 GPa, which agrees well with experimental result. Since the transverse modulus can be influenced by the alignment direction of

graphitic sheets, the modulus along both the X and Y direction is calculated. As the density increases, the modulus generally increases. For the low-density carbon fibers, there are large pores in the fiber core structure which decrease the contact area between sheets and weakens the Van der Waals interactions. The transverse moduli can also be influenced by alignment direction. As shown in Fig. 5, most of graphitic sheets aligned along Y direction for fiber core samples which results in the deformation in the X-direction increasing the interplanar spacing between the graphitic sheets by overcoming the Van der Waals interaction. However, for sheets aligned along the Y direction, the tensile force leads to slip between the graphitic sheets, which is easier than pulling the planes apart. Therefore, the transverse modulus at X direction is larger than Y direction for these samples, except for the 1.2 g/cm<sup>3</sup> fiber core, which has a very thin neck structure at X direction. Fig. 13(b–c) shows the transverse modulus in the X-direction and Y-directions for continuous and discontinuous fiber core model. Since in the discontinuous system, the lines of atoms are removed along the axial direction, the transverse modulus has a similar value for continuous and discontinuous model of same density.

Unsurprisingly, the excess volume in fiber cores accumulates in pores; thus, the porosity decreases with the increase of density. The presence of these small pores influences the properties of the fiber core models. First, they reduce the density. For the thin fiber, most of pores are healed during relaxation resulting in a final density and pore size distribution that is essentially independent of the initial density. The presence of pores influences the mechanical properties of carbon fiber. Low density fiber core samples have low tensile moduli and strength in both longitudinal and transverse directions. This is because the pores lower the number of graphene sheets per transverse cross-sectional area and thus decreases the longitudinal tensile strength and modulus. The voids also decrease the contact area between graphene sheets which are held together by weak Van der Waals forces, resulting in a lower transverse modulus.

#### 4. Conclusions

We have modeled carbon fiber using the kMC-MD algorithm and ReaxFF reactive force field. The microstructures are generated from initial eight-atom ladder units by creating bonds between unsaturated carbon atoms of different units based on the kMC-MD algorithm. Then the generated 2D microstructure is replicated in the z-direction to form fully 3D microstructures and relaxed by the physically sophisticated ReaxFF reactive force field. Fiber core and thin fiber CF models are generated by controlling the CF shape via a virtual force wall. These fiber core and thin fiber models represent a small section of the interior region of thick fiber and a very thin carbon fiber with a well-defined surface. Extensive characterization of structural features including initial packing densities, final densities of structures, pore size distribution, hybridization state, XRD analysis yielded results similar to experimental results in the literature. Moreover, the mechanical properties of this CF model were investigated, and a discontinuous CF model was proposed by removing one layer of carbon atoms at random position of each graphitic sheet; this resulted in a reduction in the tensile modulus to levels comparable to real carbon fibers. Our key findings are:

- 1 By controlling the initial packing density, the generated fiber core models can have a large range of the final density from 1.45 to 2.10 g/cm<sup>3</sup>. For initial densities up to 1.9 g/cm<sup>3</sup>, the final density of fiber increases with the increase of the initial density. The final density of 2.0 g/cm<sup>3</sup> fiber core is slightly lower than the 1.9 g/cm<sup>3</sup> fiber core. Since the free surface annihilate most of pores in thin fiber model, the final density of thin fiber model is independent to the initial packing density and the densities of

all thin fiber samples are densified to the 2.16–2.19 g/cm<sup>3</sup> after generation process.

- 2 The pore size distribution analysis shows the volume fractions of pores decreased in fiber core with the increase of the density of the initial structure while it is independent to the initial density in thin fiber.
- 3 Both core fiber and thin fiber models show similar evolution of hybridization state during the generation process. The percentage of sp hybridization decreases to below 10% while it of sp<sup>2</sup> hybridization increases to above 90% in the generation. No more than 0.1% sp<sup>3</sup> hybridized carbon atoms are observed in both fiber core and thin fibers.
- 4 XRD analysis results show the crystallite thickness  $L_c$  and crystallite correlation length  $L_a$  obtained from both fiber core and thin fiber models are consistent with experimental values in the literature, although the average crystallite thickness and correlation length among fiber models is relatively smaller than experimental values.
- 5 By introducing physically reasonable discontinuities in the structures the z-direction, the Young's modulus of discontinuous fiber core and thins fiber models are in the range of 200–400 GPa, which lies in the modulus range of PAN fiber. However, the tensile strength of discontinuous model is still 2–5 times larger than the experiment value due to the high level of alignment and the absence of other structural imperfection in the model. It should be noted that the discontinuous model reaches the axial tensile moduli comparable with experimental results. However, covalent bonds and the complex morphologies still dominate the tensile modulus in real fiber. The transverse modulus of both continuous and discontinuous fiber core models is in the range of 0.2–5 GPa which agrees well with the experimental value of transverse modulus of PAN and pitch-based CFs.
- 6 The high-density fiber core has a similar microstructure to the thin fiber because they have similar final densities. The method presented here is a good first step to the construction of a highly realistic carbon fiber model. The thin fiber model is an ideal platform in which to investigate the surface chemical reactions between carbon fibers and reactive gases, most particularly atomic and molecular oxygen. Since carbon fibers are also frequently embedded in polymer or metal matrix to form composites, the thin fiber model also provides an opportunity to investigate the interfacial properties with a matrix such as resin.

#### CRediT authorship contribution statement

**Linyuan Shi:** Methodology, Software, Investigation, Writing - original draft, Visualization. **Marina Sessim:** Writing - review & editing. **Michael R. Tonks:** Conceptualization, Resources, Writing - review & editing, Supervision. **Simon R. Phillpot:** Conceptualization, Resources, Writing - review & editing, Supervision, Data curation.

#### Declaration of competing interest

The authors declare that they have no known competing financial interests or personal relationships that could have appeared to influence the work reported in this paper.

#### Acknowledgments

This work was supported by the Early Stage Innovations (ESI) NASA Grant 80NSSC18K0250. We are grateful to Joshua Monk, Nagi Mansour and Arvind Srikanth for valuable discussions.

## Appendix A. Supplementary data

Supplementary data to this article can be found online at <https://doi.org/10.1016/j.carbon.2020.11.011>.

## References

- [1] B.A. Newcomb, Processing, structure, and properties of carbon fibers, Compos Part A Appl Sci Manuf 91 (2016) 262–282, <https://doi.org/10.1016/j.compositesa.2016.10.018>.
- [2] D.D. Edie, The effect of processing on the structure and properties of carbon fibers, Carbon N Y 36 (1998) 345–362, [https://doi.org/10.1016/S0008-6223\(97\)00185-1](https://doi.org/10.1016/S0008-6223(97)00185-1).
- [3] L. Qiu, X.H. Zheng, J. Zhu, G.P. Su, D.W. Tang, The effect of grain size on the lattice thermal conductivity of an individual polyacrylonitrile-based carbon fiber, Carbon N Y 51 (2013) 265–273, <https://doi.org/10.1016/j.carbon.2012.08.052>.
- [4] A. Jacob, Carbon fibre and cars – 2013 in review, Reinforc Plast 58 (2014) 18–19, [https://doi.org/10.1016/S0034-3617\(14\)70036-0](https://doi.org/10.1016/S0034-3617(14)70036-0).
- [5] C. Soutis, Carbon fiber reinforced plastics in aircraft construction, Mater. Sci. Eng., A 412 (2005) 171–176, <https://doi.org/10.1016/j.msea.2005.08.064>.
- [6] J. Wang, Application of composite materials on sports equipments, Appl. Mech. Mater. 155–156 (2012) 903–906. <https://doi.org/10.4028/www.scientific.net/AMM.155-156.903>.
- [7] B.K. Bessire, S.A. Lahankar, T.K. Minton, Pyrolysis of phenolic impregnated carbon ablator (PICA), ACS Appl. Mater. Interfaces 7 (2015) 1383–1395, <https://doi.org/10.1021/am507816f>.
- [8] X. Qin, Y. Lu, H. Xiao, Y. Hao, D. Pan, Improving preferred orientation and mechanical properties of PAN-based carbon fibers by pretreating precursor fibers in nitrogen, Carbon N Y 49 (2011) 4598–4600, <https://doi.org/10.1016/j.carbon.2011.06.011>.
- [9] Y. Liu, S. Kumar, Recent progress in fabrication, structure, and properties of carbon fibers, Polym. Rev. 52 (2012) 234–258, <https://doi.org/10.1080/15583724.2012.705410>.
- [10] H.G. Chae, B.A. Newcomb, P.V. Gulgulje, Y. Liu, K.K. Gupta, M.G. Kamath, et al., High strength and high modulus carbon fibers, Carbon N Y 93 (2015) 81–87, <https://doi.org/10.1016/j.carbon.2015.05.016>.
- [11] T. Kobayashi, K. Sumiya, Y. Fujii, M. Fujie, T. Takahagi, K. Tashiro, Stress-induced microstructural changes and crystallite modulus of carbon fiber as measured by X-ray scattering, Carbon N Y 50 (2012) 1163–1169, <https://doi.org/10.1016/j.carbon.2011.10.029>.
- [12] A. Gupta, I.R. Harriso, New aspects in the oxidative stabilization of pan-based carbon fibers, Carbon N Y 34 (1996) 1427–1445, [https://doi.org/10.1016/S0008-6223\(96\)00094-2](https://doi.org/10.1016/S0008-6223(96)00094-2).
- [13] X. Huang, Fabrication and properties of carbon fibers, Materials 2 (2009) 2369–2403, <https://doi.org/10.3390/ma2042369>.
- [14] B. Saha, G.C. Schatz, Carbonization in polyacrylonitrile (PAN) based carbon fibers studied by reaxff molecular dynamics simulations, J. Phys. Chem. B 116 (2012) 4684–4692, <https://doi.org/10.1021/jp300581b>.
- [15] H. Khayyam, M. Naebe, O. Zabihi, R. Zamani, S. Atkiss, B. Fox, Dynamic prediction models and optimization of polyacrylonitrile (PAN) stabilization processes for production of carbon fiber, IEEE Trans Ind Informatics 11 (2015) 887–896, <https://doi.org/10.1109/TII.2015.2434329>.
- [16] M.L. Minus, S. Kumar, The processing, properties, and structure of carbon fibers, J. Miner. Met. Mater. Soc. 57 (2005) 52–58, <https://doi.org/10.1007/s11837-005-0217-8>.
- [17] E.S. Penev, V.I. Artyukhov, B.I. Yakobson, Basic structural units in carbon fibers : atomistic models and tensile behavior, Carbon N Y 85 (2015) 72–78, <https://doi.org/10.1016/j.carbon.2014.12.067>.
- [18] K. Joshi, M.I. Arefev, L.V. Zhigilei, Generation and characterization of carbon fiber microstructure in atomistic simulations, Carbon N Y (2019), <https://doi.org/10.1016/j.carbon.2019.06.014>.
- [19] S. Desai, C. Li, T. Shen, A. Strachan, Molecular modeling of the microstructure evolution during carbon fiber processing, J. Chem. Phys. 147 (2017), <https://doi.org/10.1063/1.5000911>.
- [20] L. Martinez, R. Andrade, E.G. Birgin, J.M. Martinez, PACKMOL: a package for building initial configurations for molecular dynamics simulations, J. Comput. Chem. 30 (2009) 2157–2164.
- [21] S.L. Mayo, B.D. Olafson, W.A. Goddard, DREIDING: a generic force field for molecular simulations, J. Phys. Chem. 94 (1990) 8897–8909.
- [22] A.I. Jewett, Z. Zhuang, J.-E. Shea, Moltemplate a coarse-grained model assembly tool, Biophys. J. 104 (2013) 169a.
- [23] S. Nosé, A unified formulation of the constant temperature molecular dynamics methods, J. Chem. Phys. 81 (1984) 511–519, <https://doi.org/10.1063/1.447334>.
- [24] S. Plimpton, Fast parallel algorithms for short-range molecular dynamics, J. Comput. Phys. 117 (1995) 1–19, <https://doi.org/10.1006/JCPH.1995.1039>.
- [25] K. Chenoweth, A.C.T. van Duin, W.A. Goddard, ReaxFF reactive force field for molecular dynamics simulations of hydrocarbon oxidation, J. Phys. Chem. 112 (2008) 1040–1053, <https://doi.org/10.1021/jp709896w>.
- [26] S.P. Coleman, D.E. Spearot, L. Capolungo, Virtual diffraction analysis of Ni [0 1 0] symmetric tilt grain boundaries, Model. Simulat. Mater. Sci. Eng. 21 (2013), <https://doi.org/10.1088/0965-0393/21/5/055020>.
- [27] A. Stukowski, Visualization and analysis of atomistic simulation data with OVITO—the Open Visualization Tool, Model. Simulat. Mater. Sci. Eng. 18 (2010), 015012, <https://doi.org/10.1088/0965-0393/18/1/015012>.
- [28] Void analysis tool n.d. [https://github.com/phillpot-group\\_void\\_analyze](https://github.com/phillpot-group_void_analyze).
- [29] K. Joshi, M.I. Arefev, L.V. Zhigilei, Generation and characterization of carbon fiber microstructure in atomistic simulations, Carbon N Y 152 (2019) 396–408, <https://doi.org/10.1016/j.carbon.2019.06.014>.
- [30] S. Bougueroua, R. Spezia, S. Pezzotti, S. Vial, F. Quessette, D. Barth, et al., Graph theory for automatic structural recognition in molecular dynamics simulations, J. Chem. Phys. 149 (2018), <https://doi.org/10.1063/1.5045818>.
- [31] J. Siek, A. Lumsdaine, L.-Q. Lee, The Boost Graph Library: User Guide and Reference Manual, Addison-Wesley, 2002.
- [32] D.H. Wang, J.J. Hao, X.Q. Xing, G. Mo, Y. Gong, C.X. Lü, et al., Characterization of the nanopore structures of PAN-based carbon fiber precursors by small angle X-ray scattering, Chin. Phys. C 35 (2011) 870–874, <https://doi.org/10.1088/1674-1137/35/9/016>.
- [33] O. Paris, D. Loidl, H. Peterlik, Texture of PAN- and pitch-based carbon fibers, Carbon N Y 40 (2002) 551–555, [https://doi.org/10.1016/S0008-6223\(01\)00139-7](https://doi.org/10.1016/S0008-6223(01)00139-7).
- [34] P. Morgan, Carbon Fibers and Their Composites, vol. 210, 2005, [https://doi.org/10.1007/978-94-017-9478-7\\_5](https://doi.org/10.1007/978-94-017-9478-7_5).
- [35] B.D. Jensen, K.E. Wise, G.M. Odegard, The effect of time step, thermostat, and strain rate on ReaxFF simulations of mechanical failure in diamond, graphene, and carbon nanotube, J. Comput. Chem. 36 (2015) 1587–1596, <https://doi.org/10.1002/jcc.23970>.
- [36] J. Shi, C. Hu, J. Shen, K. Cai, J. Wang, Mechanical properties of bonded few-layered graphene via uniaxial test: a molecular dynamics simulation study, Comput. Mater. Sci. 172 (2020) 109295, <https://doi.org/10.1016/j.commatsci.2019.109295>.
- [37] S. Kumar, D.P. Anderson, A.S. Crasto, J.M. Martin, Carbon fibre compressive strength and its dependence on structure and morphology, J. Mater. Sci. (1993) 423–439, [https://doi.org/10.1016/S0140-6736\(00\)31479-9](https://doi.org/10.1016/S0140-6736(00)31479-9).
- [38] F. Liu, A.E.H. Wang, A.E.L. Xue, Effect of microstructure on the mechanical properties of PAN-based carbon fibers during high-temperature graphitization, J. Mater. Sci. 4316–22 (2008), <https://doi.org/10.1007/s10853-008-2633-y>.
- [39] Y. Wang, T. Yan, S. Wu, Y.J. Tong, A.J. Gao, L.H. Xu, Stretching deformation mechanism of polyacrylonitrile-based Carbon Fiber structure at high temperatures, Fibers Polym. 19 (2018) 751–759, <https://doi.org/10.1007/s12221-018-7988-3>.
- [40] M.J. Yu, Y.J. Bai, C.G. Wang, Y. Xu, P.Z. Guo, A new method for the evaluation of stabilization index of polyacrylonitrile fibers, Mater. Lett. 61 (2007) 2292–2294, <https://doi.org/10.1016/j.matlet.2006.08.071>.
- [41] N. Oya, D.J. Johnson, Longitudinal compressive behaviour and microstructure of PAN-based carbon fibres, Carbon N Y 39 (2001) 635–645, [https://doi.org/10.1016/S0008-6223\(00\)00147-0](https://doi.org/10.1016/S0008-6223(00)00147-0).
- [42] W. Li, D. Long, J. Miyawaki, W. Qiao, L. Ling, I. Mochida, et al., Structural features of polyacrylonitrile-based carbon fibers, J. Mater. Sci. 47 (2012) 919–928, <https://doi.org/10.1007/s10853-011-5872-2>.
- [43] M. Guigon, A. Oberlin, Heat-treatment of high tensile strength PAN-based carbon fibres: microtexture, structure and mechanical properties, Compos. Sci. Technol. 27 (1986) 1–23, [https://doi.org/10.1016/0266-3538\(86\)90060-6](https://doi.org/10.1016/0266-3538(86)90060-6).
- [44] A.H. Wazir, L. Kakakhel, Preparation and characterization of pitch-based carbon fibers, Xinxing Tan Caillao/New Carbon Mater 24 (2009) 83–88, [https://doi.org/10.1016/S1872-5805\(08\)60039-6](https://doi.org/10.1016/S1872-5805(08)60039-6).
- [45] F. Yang, G. Hu, H. He, M. Yi, Y. Ge, L. Ran, et al., Effect of amorphous carbon on the tensile behavior of polyacrylonitrile (PAN)-based carbon fibers, J. Mater. Sci. 54 (2019) 8800–8813, <https://doi.org/10.1007/s10853-018-03256-z>.
- [46] M. Ishikawa, Y. Kogo, J. Koyanagi, F. Tanaka, T. Okabe, Torsional modulus and internal friction of polyacrylonitrile- and pitch-based carbon fibers, J. Mater. Sci. 50 (2015) 7018–7025, <https://doi.org/10.1007/s10853-015-9254-z>.
- [47] T. Mori, K. Tanaka, Average stress in matrix and average elastic energy of materials with misfitting inclusions, Acta Metall. 21 (1973) 571–574, [https://doi.org/10.1016/0001-6160\(73\)90064-3](https://doi.org/10.1016/0001-6160(73)90064-3).
- [48] N. Meek, D. Penumadu, O. Hosseini, D. Harper, S. Young, T. Rials, Synthesis and characterization of lignin carbon fiber and composites, Compos. Sci. Technol. 137 (2016) 60–68, <https://doi.org/10.1016/j.compiscech.2016.10.016>.
- [49] Y. Chandra, F. Scarpa, S. Adhikari, J. Zhang, E.I. Saavedra Flores, H.X. Peng, Pullout strength of graphene and carbon nanotube/epoxy composites, Compos. B Eng. 102 (2016) 1–8, <https://doi.org/10.1016/j.compositesb.2016.06.070>.
- [50] K. Naito, Y. Tanaka, J.M. Yang, Transverse compressive properties of polyacrylonitrile (PAN)-based and pitch-based single carbon fibers, Carbon N Y 118 (2017) 168–183, <https://doi.org/10.1016/j.carbon.2017.03.031>.